A Pedestrian Indoor Navigation System Using Deep-Learning-Aided Cellular Signals and ZUPT-Aided Foot-Mounted IMUs

Ali A. Abdallah, Chi-Shih Jao, Zaher M. Kassas, and Andrei M. Shkel

***Abstract*— A signal-sensor-based indoor pedestrian navigation system is developed. The proposed system: (i) utilizes a foot-mounted inertial navigation system (INS), in which the accumulated errors are mitigated via a zero velocity update (ZUPT) approach and (ii) exploits opportunistically cellular long-term evolution (LTE) signals in a deep neural network (DNN)-based synthetic aperture navigation (SAN) framework, in which the pedestrian's motion is utilized to suppress multipath-induced errors. The proposed DNN-SAN-LTE-ZUPT-INS (DUALS) indoor pedestrian navigation system utilizes the complementary the desirable characteristics of both subsystems, coupled via two architectures: (a) loosely-coupled and (b) tightly-coupled. This paper designs and assesses both architectures experimentally in an indoor environment. The experimental study demonstrates a pedestrian traversing a trajectory of 600 m in 14 minutes, including a stationary period, straight segments, up/down the stairs, and riding in an elevator, while receiving signals from 4 LTE base stations (also known as evolved node B (eNodeB)). The proposed tightly-coupled DUALS system exhibited a 3-D position root mean-squared error (RMSE) of 1.34 m, outperforming the loosely-coupled DUALS, ZUPT-aided INS, and LTE-DNN-SAN which achieved a position RMSE of 1.38, 1.49, and 1.97 m, respectively.**

***Index Terms*— Beamforming, multipath mitigation, DNN, navigation, synthetic aperture, LTE, IMU, Zero Velocity Update.**

I. Introduction

REALIZING a system that enables accurate pedestrian navigation in unknown indoor environments without having to erect dedicated infrastructure has been an ongoing challenge for decades. This problem is becoming ever more critical for public safety (e.g., first responders [1]), as the time that people spend indoors is increasing dramatically. Virtually all solutions to-date require installing infrastructure, prior knowledge of the environment, and/or favorable conditions.

Existing navigation technologies can be categorized into sensor-based solutions, signal-based solutions, or a combination thereof [2]. Sensor-based technologies use dead reckoning processes to extract relative motion information [3]. However, these sensors provide *local* position estimates and accumulate errors unboundedly in the absence of external aiding sources.

Signal-based approaches provide *global* position estimates and overcomes the shortcomings of sensor-based systems [4]. Some signals (e.g., cellular 4G long-term evolution (LTE) and 5G) are received with sufficiently high power indoors, allowing a receiver to track them and subsequently produce navigation observables [5]. However, attenuation and multipath pose significant challenges to signal-based approaches, limiting their accuracy and availability [6].

This paper proposes a signal-sensor-based indoor navigation approach for pedestrians. The proposed approach, on one hand, exploits *downlink* LTE cellular signals opportunistically to provide a *global* position estimate, in which a deep neural network (DNN)-based synthetic aperture navigation (SAN) approach is developed to spatially mitigate multipath. On the other hand, the proposed approach uses a zero-velocity update (ZUPT)-based inertial navigation to provide more accurate short-duration *local* position estimate. This paper makes the following three contributions: (i) develop a pedestrian indoor system termed DUALS: **D**NN-S**A**N-**L**TE—Z**U**PT-IN**S**, (ii) design two integration schemes for fusing the information from the signal and sensor systems, (iii) evaluate the proposed system experimentally using real LTE signals in a multipath-rich environment. An experimental study is presented showing a pedestrian traversing a a trajectory of 600 m in 14 minutes, including a stationary period, straight segments, up/down the stairs, and riding in an elevator, with a shoe-mounted inertial measurement unit (IMU) while receiving signals from 4 LTE base stations (also known as evolved node B (eNodeB)). The proposed tightly-coupled DUALS system exhibited a 3-D position root mean-squared error (RMSE) of 1.34 m, outperforming the loosely-coupled DUALS, ZUPT-aided inertial navigation system (INS), and LTE-DNN-SAN which achieved a position RMSE of 1.38, 1.49, and 1.97 m, respectively.

The remainder of the paper is organized as follows. Section II discusses related work about: (i) synthetic aperture (SA)-based multipath mitigation and (ii) ZUPT-based inertial navigation. Section III presents a high-level block diagram of the proposed system. Section V develops the navigation framework, in which two different integration schemes: (i) loosely-coupled and (ii) tightly-coupled are presented. Section VI validates and assesses experimentally the proposed system

This work was performed under the financial assistance award 70NANB17H192 from U.S. Department of Commerce, National Institute of Standards and Technology (NIST).

The authors are with the University of California, Irvine, USA. *Corresponding author: Z. Kassas*. E-mails: abdalla2@uci.edu, chishihj@uci.edu, zkassas@ieee.org, ashkel@uci.edu.

for both integration schemes. Section VII concludes the paper.

II. Related Work

This section overviews relevant previous work in the literature that relates to the proposed system, which can be classified as: (i) SA-based multipath mitigation and (ii) ZUPT-based inertial navigation.

A. SA-Based Multipath Mitigation

The effect of multipath has been extensively studied in the literature. Multipath mitigation could be performed at the radio front-end stage using customized antennas (also known as smart antennas) [7]. Other approaches mitigate multipath at the receiver design level using advanced signal processing techniques. In [8], an adaptive estimator of the spectral parameters of incoming multipath signals using the associated signal-to-noise (SNR) for Global Positioning System (GPS) differential carrier phase measurements was developed. In [9], a cell-averaging constant false alarm rate (CA-CFAR)-based approach for adaptive calculation of the LOS detection threshold was developed. In the proposed approach, a continuous track of the noise variance is maintained to account for channel variations in dynamic environments. Other signal processing-based techniques include various correlation techniques [10]. Recent studies have considered multipath mitigation via machine learning (ML). In [11], a nonlinear ML-based model was developed to mitigate periodic GNSS multipath signals. ML has been also applied to identify non-line-of-sight (NLOS) conditions [12]. However, in multipath-rich environments, such as indoors, small-delay multipath signals tend to add constructively or propagate through a less-attenuated path, resulting in a dominant NLOS component(s) over the LOS component. Hence, the NLOS identification may be faulty or insufficient to maintain a reliable navigation solution compared to the approaches in which the non-dominant LOS component is utilized. The proposed approach utilizes the non-dominant LOS component by spatially suppressing the NLOS components and enhancing the LOS component power.

Multipath can also be mitigated via spatial discrimination of incoming signals via beamforming. Spatial discrimination can be applied to geometrically-diverse signals, which are collected using physical antenna arrays [13], [14] or via synthetic aperture navigation (SAN) frameworks [15]–[17]. Spatial discrimination techniques rely on the ability of beamforming towards the LOS direction while mitigating the multipath components.

At the receiver side, the accuracy of spatial discrimination is dependant on the performance of each beamforming stage; thus, the limiting factors of the beamforming process can be listed as: (i) the number of antenna elements, (ii) the limited ability of conventional spatial pre-filtering approaches to resolve for the correlation between the incoming spatially-correlated signals (which is the case in multipath scenarios), at a cost of decreasing the degree-of-freedom (DOF) of the system, i.e., the number of received multipath signals that could be estimated effectively, (iii) the ability of conventional model order estimators in estimating the order of the system, which is limited by the reduced DOF resulting from the pre-filtering stage, and (iv) the accuracy of conventional DOA estimators. This limitation can be related to the model representation and the limited number of features therein. In ML terminology, this is known as representation learning. A representation learning algorithm can extract the features for a task using datasets, where designing these features manually for complex nonlinear tasks may take decades and an entire community of researchers [18]. In [19], a DNN-based spatial discriminator was proposed to compensate for the limitations of conventional beamforming approaches, especially at the stages of prefiltering, model order estimation (MOE), and direction-of-arrival (DOA) estimation. The proposed LTE-DNN-SAN showed a significant improvement in positioning accuracy compared to LTE-SAN proposed in [20].

B. ZUPT-Based Inertial Navigation

The successful miniaturization of IMUs has enabled pedestrians to use INS, which performs localization by dead reckoning based on IMU measurements [21]. Due to noise and stochastic time-varying biases of MEMS-based IMUs, navigation errors of an INS accumulates quickly and can exceed several meters within just a few seconds of navigation [22], which does not meet the localization requirements of many public safety personnel, such as firefighters and first responders. To enhance the navigation performance, pedestrian INS deploys IMUs on different parts of a human body, including head [23], pocket [24], and foot [25], and utilizes local biomechanical information as an augmentation approach.

Among pedestrian INS solutions, foot-mounted INS have drawn attention for their ability to implement a Zero velocity UPdaTe (ZUPT) algorithm [26], which significantly enhances the performance of a strapdown INS. The ZUPT algorithm utilizes the biomechanical information that foot velocity of a pedestrian when on the ground during walking is very close to zero, and, therefore, the algorithm periodically resets velocity errors of the INS when the stance phase is detected [27]. The ZUPT-aided INS has been experimentally demonstrated to achieve an error of less than 1% of the traveling distance with an industrial-grade IMU [28]. Nevertheless, the ZUPT-aided INS has errors contributed from various sources, including sensor errors, modeling errors, and detection inconsistency of zero velocity events [29].

Sensor fusion solutions, which take advantage of measurements obtained from other non-inertial sensing modalities (e.g., barometer [30], ultrasonic sensors [31], [32], magnetometer [33], cameras [34], and dynamic vision sensors [35]), are popular approaches to enhance the localization performance of standalone ZUPT-aided INS. The purposes of sensor fusion solutions can be classified into two categories: 1) to improve the stance phase detection performance and 2) to bound the error growth of the estimated localization states, mitigating the sensor errors and modeling errors. In the first category, non-inertial measurements are combined with IMU measurements in a generalized likelihood ratio test (GLRT) framework to increase the accuracy of zero velocity event

detection [36]. The sensor modalities may include magnetometers [37], electromyography (EMG) [38], shoe-embedded pressure sensors [39], downward-facing radio frequency (RF) sensors [32], and dynamic vision sensors [35]. It is worth mentioning that the stance phase detection, also commonly known as the zero-velocity detection in the ZUPT-aided INS, identifies the periods of foot having contacts with the ground. During this period, pseudo measurements of zero velocity are feedback to correct the velocity state of the system. Further discussions about this topic can be found in [32].

In the second category of sensor fusion solutions, non-inertial measurements are usually stacked with the pseudo-measurements of zero velocity to form an augmented measurement vector of the extended Kalman filter (EKF). For example, barometric altimeters can be used with the ZUPT algorithm to bound the position error growth in the vertical direction [30]. To increase the observability of yaw angle estimation in the ZUPT algorithm, magnetometers are a popular choice to be integrated into the system [40], [41]. Measurements of a relative distance between two shoes obtained from a pair of shoe-mounted ultrasonic sensors have been shown to provide compensation to the yaw angle and extend the usage of ZUPT-aided INS [34], [42]. Biomechanical constraints of human bodies while performing daily pedestrian activities have also been exploited to bound the error growth in the navigation state estimation. These methods include restricting the maximum separation length between the two feet of a pedestrian [43] and fixing the relative position between the feet and the calves [44]. Besides measurements from self-contained sensors, signal-based systems, such as ultra-wideband (UWB) [45], WiFi [46], and GNSS [47], which directly or indirectly provide position information, were also studied to augment the ZUPT-based INS. Positions estimated by the augmented ZUPT-aided INS have been shown to achieve a higher global consistency and reliability in a long-term navigation task, as compared to the standalone ZUPT-based INS.

III. Proposed System

This section presents a high-level block diagram of the proposed pedestrian indoor navigation system. The proposed framework contains two main components: (i) a signal-based component that exploits LTE signals opportunistically to extract navigation observables to estimate the pedestrian's states in a global frame and (ii) a sensor-based component that produces a navigation solution in a local frame using the ZUPT-aided inertial navigation systems based on a foot-mounted IMU.

The signal-based component operates in a base/rover navigation framework. Imagine firefighters approaching the building with a fire truck outside the building. The truck is equipped with a GNSS antenna and LTE cellular antennas, which are connected to an RF front-end to down-mix signals to baseband. The baseband in-phase and quadrature components of the mixer are fed to a stationary unit denoted by "base." The base is essentially an LTE carrier phase-based receiver (e.g., [20]) that collects LTE signals from multiple carrier frequencies, transmitted by multiple LTE eNodeBs in the environment. The positions of the eNodeBs are pre-surveyed and assumed to be known. Moreover, the base is outdoors and has access to GNSS signals, so it can estimate its position. The firefighters will step into the building while equipped with a unit denoted by "rover." Each rover includes (i) a shoe-mounted IMU and (ii) a copy of the same LTE receiver used in the base unit; however, this LTE receiver is integrated with a DNN-SAN correction block in which the motion of the firefighters is utilized to synthesize a geometrically-separated antenna array from time-separated snapshots. This allows for beamforming towards the LOS from the rover to the LTE eNodeB, while suppressing multipath components. This process requires obtaining the LOS steering vector, which is obtained by taking the nearest DOA estimate from the proposed DNN-DOAE to the LOS DOA estimated using the current estimate of the rover's receiver and the known LTE eNodeB position. Further details about this stage can be found in [20]. A DNN is trained to replace three stages of the beamforming process: prefiltering, MOE, and DOA estimation. The DNN-SAN correction block refines the carrier phase estimates and feeds the refined estimate in a feedback fashion to the receiver. The "known" ranges between the base and the eNodeBs are removed and the base measurements $\{\phi_{\text{base}}^{(u)}\}_{u=1}^{U}$ are subtracted from the corresponding rover measurements $\{\phi_{\text{rov}}^{(u)}\}_{u=1}^{U}$ to eliminate the eNodeBs' clock biases, where U is the total number of eNodeBs. However, in this paper, the experimental demonstration is performed in post-processing fashion; thus, the rover was assumed to have access to the base measurements and the communication part is not discussed in the paper. In summary, the navigation filter estimates the position, velocity, orientation, and clock bias, and drift of the rover. The IMU measurements are used to propagate the states of the rover, as discussed next.

The sensor-based component produces local navigation solutions by implementing the ZUPT-based INS. A detailed discussion of the algorithm can be found in [27]. In this approach, one IMU is mounted on the shoe of a pedestrian. In the proposed implementation, the IMUs are mounted at the toe side of the shoe, and the EKF framework is used to fuse the INS solution with the ZUPT measurements. In the prediction step of the EKF, navigation states were propagated according to the standard strapdown inertial navigation systems using IMU measurements. In the update step, pseudo-measurements of zero velocity were utilized to converge the velocity states to zeros when a stance phase is automatically detected. The stance phase detector used in this paper was the stance hypothesis optimal detection (SHOE) detector. Fig. 1 presents an overview of the proposed system.

IV. DNN-Based Spatial Discrimination

This section discusses the DNN-based spatial discrimination for multipath mitigation. In conventional approaches, the spatial discrimination-based multipath mitigation process can be divided into four stages: (i) spatial smoothing (SS), (ii) MOE, (iii) DOA estimation (DOAE), and (iv) multipath mitigation. In the proposed approach, two cascaded DNNs were designed to perform two tasks : (i) prefilter data and estimate the

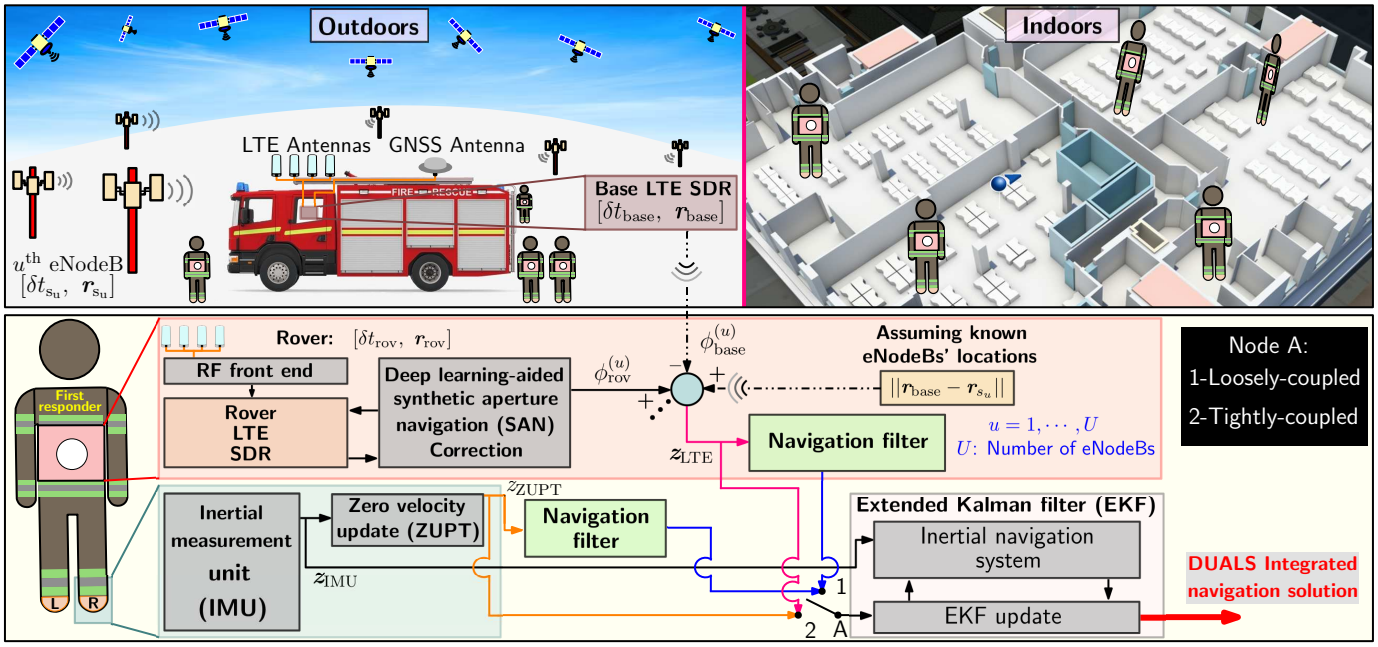

Fig. 1. Overview of the proposed system.

Fig. 2. Convectional versus DNN-based spatial discrimination.

system order and (ii) estimate the DOAs of incoming signals impinging on the synthetic antenna array, respectively. The first task is nothing but a "regression" task between the input vector $\boldsymbol{i}_1$ and a scalar output o_1. The second task depends on the output of the first task, which makes it a mix of "regression" and "semi-structured output" tasks, where input $\boldsymbol{i}_2$ and output $\boldsymbol{o}_2$ are both vectors [18]. The rest of the section discusses the training process and design of the proposed DNN-MOE and DNN-DOAE.

A. Training process

For the training process, a major challenge is to generate real datasets from real experiments due to the intractable properties of the application, where it is almost impossible to get the true order of the system and the DOA of different incoming signals in real scenarios. An alternative solution is to rely on simulating datasets that describe real scenarios as much as possible. For this purpose, the LTE simulator developed in [19] is adopted to provide high fidelity channel impulse response (CIR) estimates assuming channel parameters for an indoor office building presented in [48], [49].

B. DNN Design

DNN design requires defining the terms that characterize its performance shape such as: (i) the total number of layers in the network (excluding the input layer), (ii) the number of neurons in each layer, (iii) the total number of neurons in the network, (iv) the connections between different layer and nodes in the network, and (v) the functions that the network is capable of learning. When designing an artificial network, there is no analytical way to find the optimal number of layers and neurons for each layer. However, a decent estimate of the optimal number of layers can be chosen based on the number of sequential instructions that must be executed in the model-based approach. To address this challenge, the experimentation approach was applied to predict the model of interest, which is mainly following a sequence of experiments to discover what works the best [18].

1) DNN-MOE: Conventional MOEs, like minimum description length (MDL) criterion and Akaike information criterion (AIC), perform a 2-D clustering of the eigenvalues of the estimated data covariance matrix and divide the spanned space into two subsets: signals subspace and noise subspace. Then, the minimum depth of the proposed DNN-MOE can be achieved by a 2-layer multi-layer perceptron (MLP). However, this is assuming that the DNN is going to learn the same model, which is neither necessary nor desirable. Thus, experimentation is performed to evaluate the optimal size of the proposed network. To do so, an incremental order selection (IOS) algorithm is applied, in which the size of the DNN started with 1-2-DNN[1] and increased gradually to 50-25-DNN. For each training configuration, the samples are divided into 60% for training, 20 % for testing, and 20% for selection; where selection data is used to determine how the network performs with new data which determines the generality of the trained DNN. The normalized squared error was used as a performance metric, where the final training and selection errors were recorded for assessment. Eight datasets corresponding to $N \in \{4, 8, 12, \cdots, 32\}$ antenna array sizes were generated. Each sample in the datasets was chosen

[1] i-j-DNN denotes a DNN with j layers and i neurons in each layer

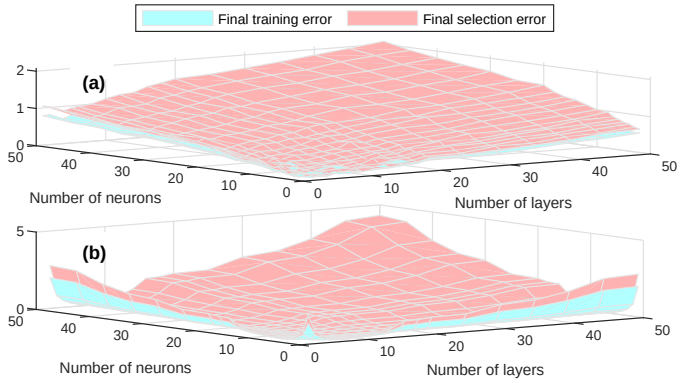

Fig. 3. The final training error and selection error of the proposed (a) DNN-MOE and (b) DNN-DOAE for different number of layers and neurons.

randomly from a uniform distribution with support 1 through N. The upper limit N was chosen to enable fair comparison with conventional model order estimators: MDL and AIC. The final selection and training errors for a specific size were averaged over the eight datasets, in order to find a sub-optimal design that is applicable to different antenna array sizes. For each dataset, the input vector $\boldsymbol{i}_{1,N}$ is of length N, and contains the eigenvalues of the estimated data covariance matrix of the LTE signals impinging on the antenna array.

Fig. 3(a) illustrates the training results, from which the following can be concluded:

- Two-layer DNNs appear to be a good design for the DNN-MOE; however, a sub-optimal performance was achieved for 4-2-DNN.
- The training and selection errors increase monotonically for the most time with the size of the DNN.
- The errors start to increase significantly as the DNN size increases, which can be attributed to oversized DNN and the overfitting of training process.

2) DNN-DOAE: For conventional DOA estimators, e.g., the standard ESPRIT algorithm, it is virtually impossible to track the number of sequential instructions required to produce DOA estimates given the eigenvectors of the data covariance matrix. This rises the importance of experimentation in designing the DNN and come up with a sub-optimal design for the proposed DNN-DOAE. The DNN-DOAE training settings are identical to that of the DNN-MOE. Fig. 3(b) illustrates the training results, from which the following can be concluded:

- The DNN-DOAE results in higher training and selection errors, which can be justified due to the nature and complexity of the task compared to the previous one. The sub-optimal performance was achieved for 5-5-DNN.
- Unlike DNN-MOE, the errors here possess a nonmonotonic behavior, where it starts high, then decreases as size increases, and at some point, it starts to increase back as the size increases. This convex shape can be justified by the high errors due to underfitting for small DNN sizes and oversized DNN for large sizes.

V. Navigation Frameworks

This section presents two navigation frameworks: (i) a loosely-coupled DUALS and (ii) a tightly-coupled DUALS. The frameworks differ in the way they fuse the shoe-mounted sensors and LTE-DNN-SAN system to produce an integrated navigation solution. For simplicity, in the EKF implementation, the loosely-coupled and tightly-coupled integration schemes are denoted by LC and TC, respectively.

A. Standalone Frameworks

A summary of the standalone LTE-DNN-SAN and ZUPT-aided INS EKF implementation is presented in this Subsection. Further details of the standalone LTE EKF implementation can be found in [50].

1) LTE-DNN-SAN Framework: An EKF is used to estimate the state vector from cellular LTE measurements $\boldsymbol{z}_{\text{LTE}}$ defined as

$$\boldsymbol{z}_{\text{LTE}} = \left[z^{(1)}, \cdots, z^{(U)}\right]^{\mathsf{T}}, \tag{1}$$

where U is the number of eNodeBs. The state vector $\boldsymbol{x}_{\text{LTE}}$ is defined as

$$\boldsymbol{x}_{\text{LTE}} \triangleq \left[\boldsymbol{r}^{\mathsf{T}}, \dot{\boldsymbol{r}}^{\mathsf{T}}, \boldsymbol{x}_{\text{clk}}^{\mathsf{T}}\right]^{\mathsf{T}} \in \mathbb{R}^{8\times 1}, \tag{2}$$

where $\boldsymbol{r}$ and $\dot{\boldsymbol{r}}$ are position and velocity, respectively, which are defined in a north-east-down (NED) Cartesian coordinate frame. The clock state vector $\boldsymbol{x}_{\text{clk}}$ is defined as

$$\begin{aligned}\boldsymbol{x}_{\text{clk}} &\triangleq \boldsymbol{x}_{\text{clk}_{\text{rov}}} - \boldsymbol{x}_{\text{clk}_{\text{base}}} \\ &= \left[c(\delta t_{\text{rov}} - \delta t_{\text{base}}), c(\dot{\delta t}_{\text{rov}} - \dot{\delta t}_{\text{base}})\right]^{\mathsf{T}},\end{aligned} \tag{3}$$

where δt_{rx_i} and $\dot{\delta t}_{\text{rx}_i}$ are the clock bias and drift of the i-th receiver, respectively, where $\text{rx} \in \{\text{rov}, \text{base}\}$; and c is the speed of light. The rover's motion is assumed to evolve according to a nearly constant velocity dynamics with a discrete-time state transition matrix and process noise covariance matrix denoted by $\mathbf{F}_{\text{rov}}$ and $\mathbf{Q}_{\text{rov}}$, respectively. The clock error dynamics are assumed to evolve according to standard double integrator model with a discrete-time state transition matrix and process noise covariance matrix denoted by $\mathbf{F}_{\text{clk}}$ and $\mathbf{Q}_{\text{clk}} \triangleq \mathbf{Q}_{\text{clk}_{\text{nav}}} + \mathbf{Q}_{\text{clk}_{\text{base}}}$, respectively. The propagated state vector and the corresponding covariance matrix are denoted by $\hat{\boldsymbol{x}}_{\text{LTE}}(k|j)$ and $\mathbf{P}_{\text{LTE}}(k|j)$, respectively, where k and j are discrete-time instances such that $k > j$. It is worth mentioning that the LTE navigation observables are obtained at the LTE OFDM frame rate which is 100 Hz [51].

Once an LTE measurement is received, an EKF measurement update is performed. The LTE measurement Jacobian is defined as

$$\mathbf{H}_{\text{LTE}}(k) = \left[\boldsymbol{H}^{(1)^{\mathsf{T}}}(k), \cdots, \boldsymbol{H}^{(U)^{\mathsf{T}}}(k)\right]^{\mathsf{T}}, \tag{4}$$

$$\boldsymbol{H}^{(u)}(k) = \left[\frac{[\hat{\boldsymbol{r}}(k|j) - \boldsymbol{r}_{s,u}]^{\mathsf{T}}}{\|\hat{\boldsymbol{r}}(k|j) - \boldsymbol{r}_{s,u}\|_2}, \mathbf{0}_{1\times 3}, 1, 0\right],$$

where $\{\boldsymbol{r}_{s,u}\}_{u=1}^{U}$ are the LTE eNodeBs locations in the NED coordinate frame. The LTE measurement noise covariance matrix $\mathbf{R}_{\text{LTE}}$ at instance k is defined as

$$\mathbf{R}_{\text{LTE}}(k) = \text{diag}\left[\sigma_1^2(k), \cdots, \sigma_U^2(k)\right],$$

where $\left\{\sigma^2{}_u(k)\right\}_{u=1}^{U}$ are tuned to be inversely proportional to the carrier-to-noise (C/N_0) ratio for the u-th eNodeB as dicussed in [52].

2) ZUPT-aided INS Framework: ZUPT-aided INS uses an EKF to estimate the pedestrian's state vector $\boldsymbol{x}_{\text{ped}}$ defined as

$$\boldsymbol{x}_{\text{ped}} \triangleq \left[\boldsymbol{q}^{\mathsf{T}}, \dot{\boldsymbol{r}}^{\mathsf{T}}, \boldsymbol{r}^{\mathsf{T}}, \boldsymbol{b}_a{}^{\mathsf{T}}, \boldsymbol{b}_g{}^{\mathsf{T}}\right]^{\mathsf{T}} \in \mathbb{R}^{15\times 1}, \tag{5}$$

where $\boldsymbol{q}$ is attitude states expressed in quaternion, which is a 3×1 vector instead of 4×1 as a result of alttitude error calculation [27]. $\boldsymbol{b}_a$, and $\boldsymbol{b}_g$ are accelerometers biases, and gyroscope biases of a foot-mounted IMU, respectively. The ZUPT-aided INS discrete-time propagation function, state transition matrix, the corresponding process noise covariance matrix, propagated state vector, and the corresponding covariance matrix are denoted by $\boldsymbol{f}_{\text{ped}}(k|j)$, $\mathbf{F}_{\text{ped}}(k|j)$, $\mathbf{Q}_{\text{ped}}(k|j)$, $\hat{\boldsymbol{x}}_{\text{ped}}(k|j)$, and $\mathbf{P}_{\text{ped}}(k|j)$, respectively.

Once a ZUPT event is detected by a stance phase detector, the system feeds back a pseudo-velocity-measurement vector $\boldsymbol{z}_{\text{ZUPT}} = \mathbf{0}_{3\times 1}$. The ZUPT measurement covariance matrix is set as $\mathbf{R}_{\text{ZUPT}} = \text{diag}[\epsilon^2, \epsilon^2, \epsilon^2]$, where ϵ is a small value representing fictitious measurement noise variance determined according to the pedestrian's activity (e.g., walking, running, etc.). In this paper, the SHOE detector for the stance phase detection is used [36]. The ZUPT measurement matrix $\mathbf{H}_{\text{ZUPT}}$ of the update step is given by

$$\mathbf{H}_{\text{ZUPT}} = \begin{bmatrix}\mathbf{0}_{3\times 3} & \mathbf{I}_{3\times 3} & \mathbf{0}_{3\times 9}\end{bmatrix}.$$

Further details of the standalone ZUPT-aided INS EKF implementation can be found in [27].

B. Loosely-Coupled DUALS

In the loosely-coupled architecture, the standalone LTE navigation solution is used to aid the shoe-mounted sensors. The proposed loosely-coupled navigation solution is obtained by fusing the LTE's position estimate in the measurement update of the ZUPT-aided INS EKF discussed in Subsection V-A.2. The advantage of using a loose-coupling architecture is to extract desirable attributes from both sub-systems while suppressing the undesirable attributes of each, i.e., the loosely-coupled DUALS navigation solution features the relatively-short-term accuracy of the shoe-mounted system in the local frame and the bounded errors of the LTE system in a global frame.

The EKF estimates the state vector $\boldsymbol{x}_{\text{LC}} \triangleq \boldsymbol{x}_{\text{ped}}$ defined in (5). The propagation step is exactly the same as the standalone ZUPT-aided INS framework and the propagated state vector and the corresponding covariance matrix are denoted by $\hat{\boldsymbol{x}}_{\text{LC}}(k|j)$ and $\mathbf{P}_{\text{LC}}(k|j)$, respectively. However, in the measurement update, the LC measurement vector is defined as

$$\boldsymbol{z}_{\text{LC}}(k) \triangleq \left[\boldsymbol{z}_{\text{ZUPT}}^{\mathsf{T}}(k), \hat{\boldsymbol{r}}_{\text{LTE}}^{\mathsf{T}}(k)\right]^{\mathsf{T}}, \tag{6}$$

where $\hat{\boldsymbol{r}}_{\text{LTE}}^{\mathsf{T}}$ is the standalone LTE estimated position as discussed in Subsection V-A.1. To this end, a measurement update is performed according to

$$\hat{\boldsymbol{x}}_{\text{LC}}(k|k) = \hat{\boldsymbol{x}}_{\text{LC}}(k|j) + \mathbf{K}_{\text{LC}}(k)\boldsymbol{\nu}_{\text{LC}}(k), \tag{7}$$

where $\boldsymbol{\nu}_{\text{LC}}$ and $\mathbf{K}_{\text{LC}}$ are the innovation vector and Kalman gain, respectively, given by

$$\boldsymbol{\nu}_{\text{LC}}(k) \triangleq \boldsymbol{z}_{\text{LC}}(k) - \hat{\boldsymbol{z}}_{\text{LC}}(k|j), \tag{8}$$

$$\hat{\boldsymbol{z}}_{\text{LC}}(k|j) = \left[\hat{\dot{\boldsymbol{r}}}^{\mathsf{T}}(k|j), \hat{\boldsymbol{r}}^{\mathsf{T}}(k|j)\right]^{\mathsf{T}} \tag{9}$$

$$\mathbf{K}_{\text{LC}}(k) \triangleq \mathbf{P}_{\text{LC}}(k|j)\mathbf{H}_{\text{LC}}^{\mathsf{T}}(k)\mathbf{S}_{\text{LC}}^{-1}(k), \tag{10}$$

$$\mathbf{S}(k) \triangleq \mathbf{H}_{\text{LC}}(k)\mathbf{P}_{\text{LC}}(k|j)\mathbf{H}_{\text{LC}}^{\mathsf{T}}(k) + \mathbf{R}_{\text{LC}}(k), \tag{11}$$

where $\mathbf{R}_{\text{LC}}$ is the LC measurement noise covariance matrix given by $\mathbf{R}_{\text{LC}}(k) = \text{blkdiag}\left[\mathbf{R}_{\text{ZUPT}}, \mathbf{P}_{\text{LTE},\boldsymbol{r}_{\text{rov}}}(k|k)\right]$ and $\mathbf{H}_{\text{LC}}$ the LC Jacobian matrix defined as

$$\mathbf{H}_{\text{LC}}(k) = \left[\mathbf{H}_{\text{ZUPT}}^{\mathsf{T}}(k) \;\; \mathbf{H}_{\text{LTE,LC}}^{\mathsf{T}}\right]^{\mathsf{T}}, \tag{12}$$

$$\mathbf{H}_{\text{LTE,LC}} = \left[\mathbf{0}_{3\times 6} \;\; \mathbf{I}_{3\times 3} \;\; \mathbf{0}_{3\times 6}\right]. \tag{13}$$

The estimation error covariance matrix is updated according to

$$\mathbf{P}_{\text{LC}}(k|k) = \left[\mathbf{I} - \mathbf{K}_{\text{LC}}(k)\mathbf{H}_{\text{LC}}(k)\right]\mathbf{P}_{\text{LC}}(k|j). \tag{14}$$

Fig. 4 depicts the loosely-coupled navigation framework, where node A is connected to 1.

C. Tightly-Coupled DUALS

In the tightly-coupled architecture, the measurement produced by the shoe-mounted sensors and LTE receivers are fused to produce a single navigation solution. In general, and in the case of pseudoranges and IMU measurements only, the tight architecture provides a more accurate solution than loose integration as established in the navigation literature [53]. However, it is hard to assume the same behavior in our systems due to the presence of other types of observables in the measurement update. Although the tight-coupling looses the redundancy that results from having two independent navigation solutions when compared to the loose-coupling, it can exploit any number of LTE pseudorange measurements available in the environment (even if it is a single measurement).

The EKF estimates the state vector $\boldsymbol{x}_{\text{TC}} \triangleq \left[\boldsymbol{x}_{\text{ped}}^{\mathsf{T}}, \boldsymbol{x}_{\text{clk}}^{\mathsf{T}}\right]^{\mathsf{T}}$, where $\boldsymbol{x}_{\text{clk}}$ is defined in (3). The TC state transition and process noise covariance matrices are defined as $\mathbf{F}_{\text{TC}} = \text{blkdiag}\left[\mathbf{F}_{\text{ped}}, \mathbf{F}_{\text{clk}}\right]$ and $\mathbf{Q}_{\text{TC}} = \text{blkdiag}\left[\mathbf{Q}_{\text{ped}}, \mathbf{Q}_{\text{clk}}\right]$, respectively. The propagated state vector and the corresponding covariance matrix are denoted by $\hat{\boldsymbol{x}}_{\text{TC}}(k|j)$ and $\mathbf{P}_{\text{TC}}(k|j)$, respectively.

In the measurement update, the TC measurement vector is defined as

$$\boldsymbol{z}_{\text{TC}} = \left[\boldsymbol{z}_{\text{ZUPT}}^{\mathsf{T}}, \boldsymbol{z}_{\text{LTE}}^{\mathsf{T}}\right]^{\mathsf{T}}. \tag{15}$$

To this end, a measurement update is performed according to the same equations in (7-11) except for

$$\hat{\boldsymbol{z}}_{\text{TC}}(k|j) = \left[\hat{\dot{\boldsymbol{r}}}^{\mathsf{T}}(k|j), \hat{z}^{(1)}, \cdots, \hat{z}^{(U)}\right]^{\mathsf{T}} \tag{16}$$

$$\hat{z}^{(u)} = \left\|\hat{\boldsymbol{r}}(k|j) - \boldsymbol{r}_{s,u}\right\|_2 + c\hat{\delta}t \tag{17}$$

$$\mathbf{H}_{\text{TC}}(k) = \left[\mathbf{H}_{\text{ZUPT}}^{\mathsf{T}}(k) \;\; \mathbf{H}_{\text{LTE}}^{\mathsf{T}}(k)\right]^{\mathsf{T}}, \tag{18}$$

$$\mathbf{R}_{\text{TC}}(k) = \text{blkdiag}\left[\mathbf{R}_{\text{ZUPT}}, \mathbf{R}_{\text{LTE}}(k)\right]. \tag{19}$$

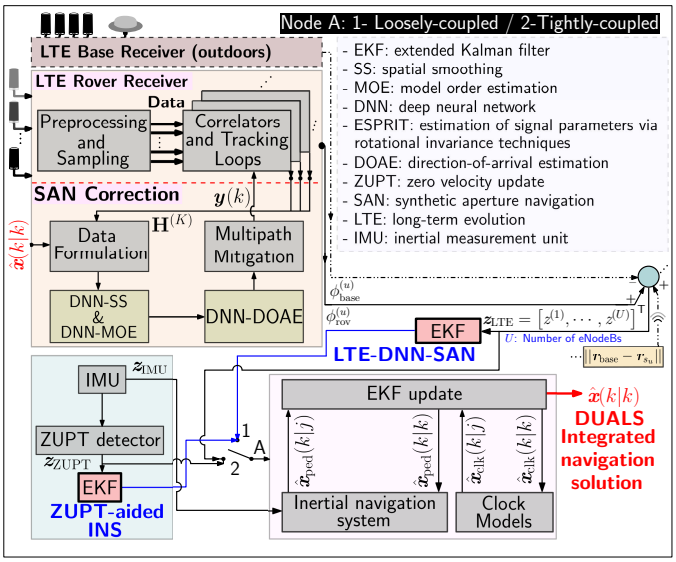

Fig. 4. The proposed navigation framework.

The estimation error covariance matrix is updated according to (14). Fig. 4 depicts the tightly-coupled navigation framework, where node A is connected to 2.

VI. Experimental Results

This section presents experimental results to evaluate the performance of the DUALS integrated navigation system for both integration schemes.

A. Experimental Setup and Environmental Layout

The experiment was conducted at the Engineering Gateway (EG) building at the University of California, Irvine, USA. The pedestrian-mounted received signals from three U.S. cellular providers: T-Mobile, Verizon, and AT&T, transmitting at four different frequencies. The locations of the LTE eNodeBs relative to the building are shown in Fig. 5(b). The receiver was equipped with four consumer-grade cellular omni-directional Laird antennas and a quad-channel National Instruments (NI) universal software radio peripheral (USRP)-2955 to simultaneously down-mix and synchronously sample LTE signals at 10 Msps. The LTE eNodeBs' characteristics are summarized in Table I. The pedestrian's shoe was mounted with a tactical-grade Analog IMU Device ADIS16497-3 [54]. It is worth mentioning that the sampling rate of the IMU and LTE measurements were 1000 Hz and 100 Hz, respectively. To synchronize both sensors' measurements, the USRP-2955 was programmed to register the time stamp of the first LTE sample. For the IMU, the time stamps provided are in local time frame; however, the initial time shift is determined using the local time of the laptop, which is synchronized to an internet time server. Fig. 6 shows the experimental setup. The pedestrian's ground truth was obtained using a combination of manually-marked check points in the building and a post-processing of a video that was while the agent was performing the experiment. The pedestrian's trajectory is mapped into a highly-accurate 3D point cloud map of the EG building, which was produced using a Lidar-camera scanning system. Fig. 5(a) shows the 3D map along with the traversed trajectory, where the only 10% of the points are shown to be able to visualize the trajectory between walls.

TABLE I
LTE ENODEBS' CHARACTESTICS

eNodeB	Carrier frequency [MHz]	N_{ID}^{Cell}	Bandwidth [MHz]	Cellular provider
1	2125	223	20	Verizon
2	1955	11	20	AT&T
3	2145	441	20	T-Mobile
4	2112.5	401	20	AT&T

B. Results

Before starting the experiment, the foot-mounted IMU was calibrated by standing stationary for 30 seconds on the ground while implementing the ZUPT algorithm to estimate the initial biases of the 3-axis accelerometers and the x-and y- axes gyroscopes. The initial bias of the z-axis gyroscope was estimated by taking the average of the measurements collected during the calibration period. It was assumed that the pedestrian entered the building from outside and had access to GNSS signals at $k = 0$ and $k = 1$. This allows the pedestrian to estimate its position and initialize its state vector, including the clock bias and drift. As the pedestrian started moving, the rover started producing LTE navigation observables from the eNodeBs presented in Table I. The pedestrian traversed a 600 m trajectory in 14 minutes, which includes terrains of flat surfaces, slopes, stairs, and an elevator.

TABLE II
INDOOR POSITIONING PERFORMANCE COMPARISON

Framework	3D RMSE [m]	2D RMSE [m]	3D *FE or °ME [m]	2D *FE or °ME [m]
LTE	1.97	1.65	°7.74	°7.52
ZUPT	1.49	1.24	*1.32	*1.11
LC-DUALS	1.38	1.1	*1.35	*1.15
TC-DUALS	1.34	1.05	*1.08	*0.82

FE: Final error —- ME: Maximum error

Table II and Fig. 7 compare the performance of the different navigation frameworks: (i) standalone LTE-DNN-SAN, (ii) standalone ZUPT-aided INS, (iii) loosely-coupled DUALS, and (iv) tightly-coupled DUALS.

C. Discussion

Among the different navigation frameworks, it can be seen that the tightly-coupled DUALS outperformed the other three frameworks achieving the a 3-D position RMSE of about 1.34 m compared to 1.38, 1.49, and 1.97 m, with the loosely-coupled DUALS, ZUPT-aided INS, and LTE-DNN-SAN frameworks, respectively. Nevertheless, the performance of all frameworks is very comparable and accurate enough for many practical applications. The standalone LTE framework exhibits 3-D errors up to 7.74 m. The tightly-coupled framework performed better than the loosely-coupled framework, in which the LTE measurement update rate was set to $T_{\text{LC}} \triangleq$

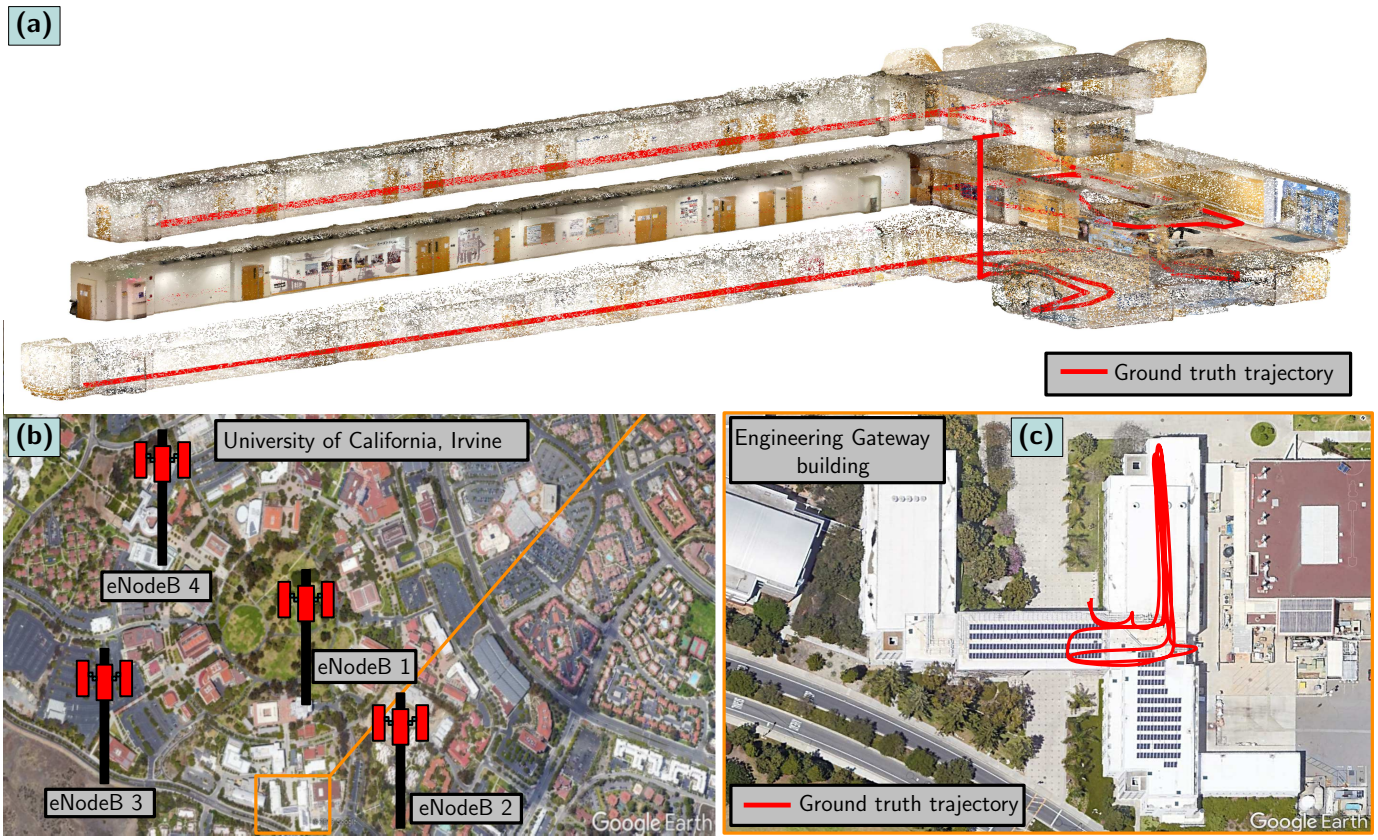

Fig. 5. Environmental layout: (a) Lidar/camera-based 3D point cloud map of the Engineering Gateway (EG) building, (b) LTE eNodeBs' positions, and (c) a satellite view of the EG building. Images: Google Earth and MATLAB.

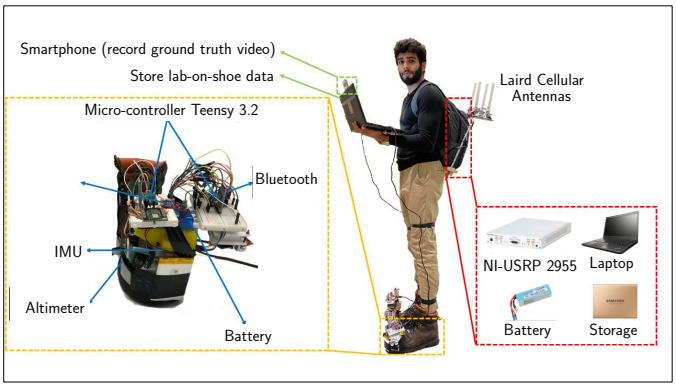

Fig. 6. Experimental software and hardware setup.

0.5 Hz due to the high correlation observed in the position estimates of the LTE-DNN-SAN EKF. The standalone ZUPT-aided INS framework exhibited an accurate navigation solution for a total duration of 14 minutes. It is worth mentioning that 85 seconds of this duration was stationary, where ZUPT-aiding is very powerful in constraining the velocity errors. Given this, it is worth mentioning that the short-time accurate velocity estimates of the ZUPT-aided INS can be exploited to enhance the formation of the synthesized antenna array; consequently, improve the multipath suppression in the beamforming stage. Yet, the performance of the presented standalone ZUPT-aided INS framework significantly outperforms the up-to-date ZUPT approaches, which exhibit around 1% accumulated position errors relative to the traversed trajectory [55] (i.e., 6 m compared to 1.34 m achieved in the proposed approach). To this end, only a relatively small improvement was showcased by aiding the ZUPT-aided INS approach with LTE signals. However, the errors of the ZUPT-aided INS are expected to keep growing with time, in which case the LTE aiding will bound the error growth enabling navigation over much longer periods indoors.

VII. Conclusion

This paper presented a **D**NN-S**A**N-**L**TE—Z**U**PT-INS (DUALS) indoor pedestrian navigation system. The proposed system uses: (i) LTE signals with a DNN-SAN approach in a base/rover framework and (ii) shoe-mounted IMU measurements enhanced by the ZUPT algorithm. DUALS benefits from the *local* accuracy attributed to ZUPT-aided INS while bounding the dead-reckoning *global* position errors provided by LTE-DNN-SAN carrier phase measurements. The system is designed and assessed for two integration architectures: loosely-coupled architecture and tightly-coupled architecture. An experiment was conducted in a multipath-rich indoor environment, in which a pedestrian traversed a distance of 600 m in 14 minutes, while equipped with a shoe-mounted IMU and receiving signals from 4 LTE eNodeBs. The tightly-coupled DUALS exhibited a 3-D position RMSE of 1.34 m and outperformed the loosely-coupled DUALS, ZUPT-aided

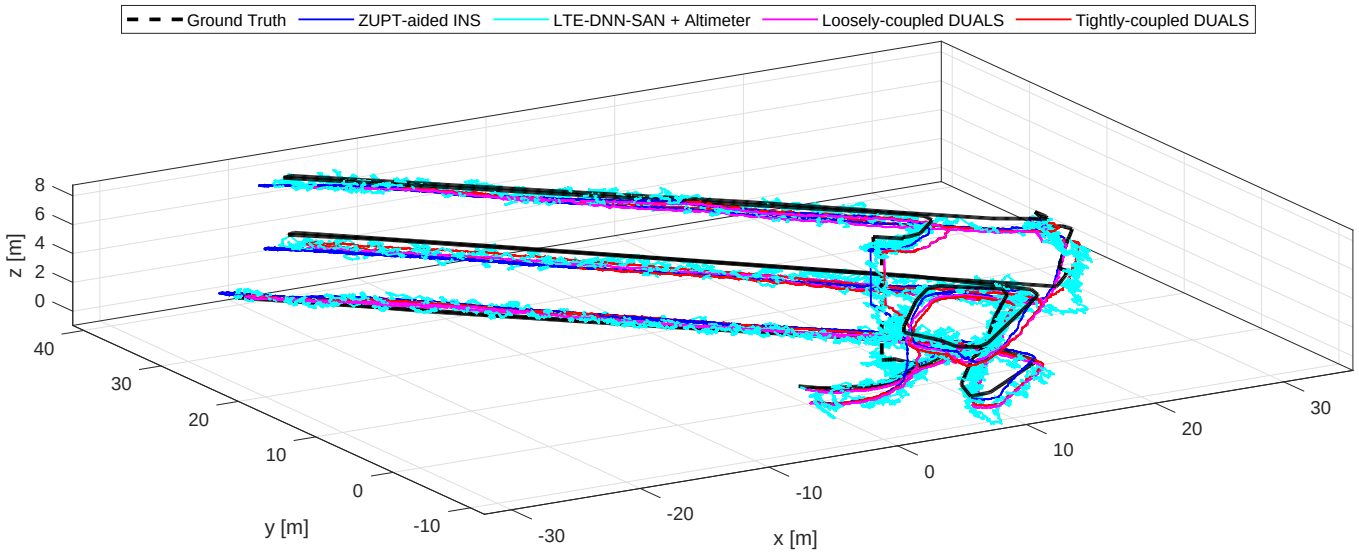

Fig. 7. The pedestrian's ground truth trajectory versus the navigation solution from: (i) Standalone LTE-DNN-SAN, (ii) Standalone ZUPT-aided INS, (iii) loosely-coupled DUALS, and (iv) tightly-coupled DUALS.

INS, and LTE-DNN-SAN with position RMSE of 1.38, 1.49, and 1.97 m, respectively.

VIII. Acknowledgment

The authors would like to thank Joe Khalife for the helpful discussions.

References

[1] V. Renaudin, O. Yalak, P. Tomé, and B. Merminod, "Indoor navigation of emergency agents," *European Journal of Navigation*, vol. 5, pp. 36–45, 2007.

[2] F. Potortì, F. Palumbo, and A. Crivello, "Sensors and sensing technologies for indoor positioning and indoor navigation," 2020.

[3] Y. Wang, S. Askari, and A. M. Shkel, "Study on mounting position of IMU for better accuracy of ZUPT-aided pedestrian inertial navigation," in *IEEE International Symposium on Inertial Sensors and Systems*, April 2019, pp. 1–4.

[4] J. Khalife and Z. Kassas, "Opportunistic UAV navigation with carrier phase measurements from asynchronous cellular signals," *IEEE Transactions on Aerospace and Electronic Systems*, vol. 56, no. 4, pp. 3285–3301, August 2020.

[5] A. Abdallah, J. Khalife, and Z. Kassas, "Experimental characterization of received 5G signals carrier-to-noise ratio in indoor and urban environments," in *Proceedings of IEEE Vehicular Technology Conference*, April 2021, pp. 1–5.

[6] X. Chen, F. Dovis, S. Peng, and Y. Morton, "Comparative studies of GPS multipath mitigation methods performance," *IEEE Transactions on Aerospace and Electronic Systems*, vol. 49, no. 3, pp. 1555–1568, July 2013.

[7] C. Counselman, "Multipath-rejecting GPS antennas," *Proceedings of the IEEE*, vol. 1, pp. 86–91, 99 1999.

[8] C. Comp and P. Axelrad, "Adaptive SNR-based carrier phase multipath mitigation technique," *IEEE Transactions on Aerospace and Electronic Systems*, vol. 34, no. 1, pp. 264–276, January 1998.

[9] K. Shamaei, J. Khalife, and Z. Kassas, "Exploiting LTE signals for navigation: Theory to implementation," *IEEE Transactions on Wireless Communications*, vol. 17, no. 4, pp. 2173–2189, April 2018.

[10] K. Shamaei and Z. Kassas, "LTE receiver design and multipath analysis for navigation in urban environments," *NAVIGATION, Journal of the Institute of Navigation*, vol. 65, no. 4, pp. 655–675, December 2018.

[11] H. Phan and S. Tan, "Mitigation of gps periodic multipath using non-linear regression," in *Proceedings of IEEE European Signal Processing Conference*, August 2011, pp. 1795–1799.

[12] X. Cai, X. Li, R. Yuan, and Y. Hei, "Identification and mitigation of NLOS based on channel state information for indoor WiFi localization," in *Proceedings of International Conference on Wireless Communications Signal Processing*, October 2015, pp. 1–5.

[13] Z. Chen, G. Gokeda, and Y. Yu, *Introduction to Direction-of-arrival Estimation*. Artech House, 2010.

[14] K. Shamaei and Z. Kassas, "A joint TOA and DOA acquisition and tracking approach for positioning with LTE signals," *IEEE Transactions on Signal Processing*, pp. 2689–2705, 2021.

[15] S. Draganov, M. Harlacher, L. Haas, M. Wenske, and C. Schneider, "Synthetic aperture navigation in multipath environments," *IEEE Wireless Communications*, vol. 18, no. 2, pp. 52–58, April 2011.

[16] S. Daneshmand, A. Broumandan, N. Sokhandan, and G. Lachapelle, "GNSS multipath mitigation with a moving antenna array," *IEEE Transactions on Aerospace and Electronic Systems*, vol. 49, no. 1, pp. 693–698, January 2013.

[17] A. Abdallah and Z. Kassas, "Evaluation of feedback and feedforward coupling of synthetic aperture navigation with LTE signals," in *Proceedings of IEEE Vehicular Technology Conference*, September 2019, pp. 1–6.

[18] I. Goodfellow, Y. Bengio, and A. Courville, *Deep learning*. Cambridge, USA: MIT press, 2016.

[19] A. Abdallah and Z. Kassas, "Deep learning-aided spatial discrimination for multipath mitigation," in *Proceedings of IEEE/ION Position, Location, and Navigation Symposium*, April 2020, pp. 1324–1335.

[20] A. Abdallah, K. Shamaei, and Z. Kassas, "Indoor localization with LTE carrier phase measurements and synthetic aperture antenna array," in *Proceedings of ION GNSS Conference*, September 2019, pp. 2670–2679.

[21] C. Tjhai and K. O'Keefe, "Comparing heading estimates from multiple wearable inertial and magnetic sensors mounted on lower limbs," in *Proceedings of International Conference on Indoor Positioning and Indoor Navigation*, 2018, pp. 206–212.

[22] M. Ming, Q. Song, Y. Li, and Z. Zhou, "A zero velocity intervals detection algorithm based on sensor fusion for indoor pedestrian navigation," in *Proceedings of IEEE Information Technology, Networking, Electronic and Automation Control Conference*, 2017, pp. 418–423.

[23] S. Beauregard, "A helmet-mounted pedestrian dead reckoning system," in *Proceedings of International Forum on Applied Wearable Computing*, 2006, pp. 1–11.

[24] E. Diaz, "Inertial pocket navigation system: Unaided 3D positioning," *Sensors*, vol. 15, no. 4, pp. 9156–9178, 2015.

[25] J. Nilsson, A. Gupta, and P. Händel, "Foot-mounted inertial navigation made easy," in *Proceedings of International Conference on Indoor Positioning and Indoor Navigation*, 2014, pp. 24–29.

[26] A. Jimenez, F. Seco, C. Prieto, and J. Guevara, "A comparison of pedestrian dead-reckoning algorithms using a low-cost MEMS IMU,"

in *Proceedings of IEEE International Symposium on Intelligent Signal Processing*, 2009, pp. 37–42.
[27] Y. Wang, A. Chernyshoff, and A. Shkel, "Error analysis of ZUPT-aided pedestrian inertial navigation," in *Proceedings of International Conference on Indoor Positioning and Indoor Navigation*, 2018, pp. 206–212.
[28] Y. Wang, Y. Lin, S. Askari, C. Jao, and A. Shkel, "Compensation of systematic errors in ZUPT-aided pedestrian inertial navigation," in *Proceedings of IEEE/ION Position, Location, and Navigation Symposium*, 2020, pp. 1452–1456.
[29] J. Wahlstrom and I. Skog, "Fifteen years of progress at zero velocity: A review," *IEEE Sensors Journal*, 2020.
[30] C. Jao, Y. Wang, S. Askari, and A. Shkel, "A closed-form analytical estimation of vertical displacement error in pedestrian navigation," in *Proceedings of IEEE/ION Position, Location and Navigation Symposium*, 2020, pp. 793–797.
[31] Y. Wang, s. Askari, C. Jao, and A. Shkel, "Directional ranging for enhanced performance of aided pedestrian inertial navigation," in *Proceedings of International Symposium on Inertial Sensors and Systems*, 2019, pp. 1–2.
[32] C. Jao, Y. Wang, and A. Shkel, "A zero velocity detector for foot-mounted inertial navigation systems aided by downward-facing range sensor," in *Proceedings of IEEE Sensors Conference*, 2020, pp. 1–4.
[33] X. Cui, Y. Li, Q. Wang, M. Zhang, and J. Li, "Three-axis magnetometer calibration based on optimal ellipsoidal fitting under constraint condition for pedestrian positioning system using foot-mounted inertial sensor/magnetometer," in *Proceedings of IEEE/ION Position, Location, and Navigation Symposium*, April 2018, pp. 166–174.
[34] C. Jao, Y. Wang, and A. Shkel, "Pedestrian inertial navigation system augmented by vision-based foot-to-foot relative position measurements," in *Proceedings of IEEE/ION Position, Location, and Navigation Symposium*, 2020, pp. 900–907.
[35] C. Jao, K. Stewart, J. Conradt, E. Neftci, and A. Shkel, "Zero velocity detector for foot-mounted inertial navigation system assisted by a dynamic vision sensor," in *Proceedings of DGON Inertial Sensors and Systems Symposium*, 2020, pp. 1–8.
[36] I. Skog, P. Handel, J. Nilsson, and J. Rantakokko, "Zero-velocity detection-an algorithm evaluation," *IEEE Transactions on Biomedical Engineering*, vol. 57, no. 11, pp. 2657–2666, 2010.
[37] A. Norrdine, K. Z, and J. Blankenbach, "Step detection for ZUPT-aided inertial pedestrian navigation system using foot-mounted permanent magnet," *IEEE Sensors Journal*, vol. 16, no. 17, pp. 6766–6773, 2016.
[38] Q. Wang, X. Zhang, X. Chen, R. Chen, W. Chen, and Y. Chen, "A novel pedestrian dead reckoning algorithm using wearable EMG sensors to measure walking strides," in *Proceedings of Ubiquitous Positioning Indoor Navigation and Location Based Service*, 2010, pp. 1–8.
[39] M. Ma, Q. Song, Y. Gu, Y. Li, and Z. Zhou, "An adaptive zero velocity detection algorithm based on multi-sensor fusion for a pedestrian navigation system," *Sensors*, vol. 18, no. 10, p. 3261, 2018.
[40] M. Kok and A. Solin, "Scalable magnetic field SLAM in 3D using Gaussian process maps," in *Proceedings of International Conference on Information Fusion*, 2018, pp. 1353–1360.
[41] Q. Wang, Z. Guo, Z. Sun, X. Cui, and K. Liu, "Research on the forward and reverse calculation based on the adaptive zero-velocity interval adjustment for the foot-mounted inertial pedestrian-positioning system," *Sensors*, vol. 18, no. 5, p. 1642, 2018.
[42] M. Placer and S. Kovačič, "Enhancing indoor inertial pedestrian navigation using a shoe-worn marker," *Sensors*, vol. 13, no. 8, pp. 9836–9859, 2013.
[43] W. Shi, Y. Wang, and Y. Wu, "Dual MIMU pedestrian navigation by inequality constraint Kalman filtering," *Sensors*, vol. 17, no. 2, pp. 427–439, 2017.
[44] H. Ju, J. L. Hong, and C. Park, "Pedestrian dead reckoning system using dual IMU to consider heel strike impact," in *Proceedings of International Conference on Control, Automation and Systems*, 2018, pp. 1307–1309.
[45] H. Benzerrouk and A. Nebylov, "Robust IMU/UWB integration for indoor pedestrian navigation," in *Proceedings of Saint Petersburg International Conference on Integrated Navigation Systems*, 2018, pp. 1–5.
[46] Y. Zhuang, H. Lan, Y. Li, and N. El-Sheimy, "PDR/INS/WiFi integration based on handheld devices for indoor pedestrian navigation," *Micromachines*, vol. 6, no. 6, pp. 793–812, 2015.
[47] H. Lan, C. Yu, and N. El-Sheimy, "An integrated PDR/GNSS pedestrian navigation system," in *Proceedings of China Satellite Navigation Conference*. Springer, 2015, pp. 677–690.
[48] A. Kaya and D. Calin, "Modeling three dimensional channel characteristics in outdoor-to-indoor LTE small cell environments," in *Proceedings of IEEE Military Communications Conference*, November 2013, pp. 933–938.
[49] Y. Wang, W. Lu, and H. Zhu, "Propagation characteristics of the LTE indoor radio channel with persons at 2.6 GHz," *IEEE Antennas and Wireless Propagation Letters*, vol. 12, pp. 991–994, 2013.
[50] A. Abdallah, K. Shamaei, and Z. Kassas, "Indoor positioning based on LTE carrier phase measurements and an inertial measurement unit," in *Proceedings of ION GNSS Conference*, September 2018, pp. 3374–3384.
[51] 3GPP, "Evolved universal terrestrial radio access (E-UTRA); physical channels and modulation," 3rd Generation Partnership Project (3GPP), TS 36.211, January 2011. [Online]. Available: http://www.3gpp.org/ftp/Specs/html-info/36211.htm
[52] A. Abdallah, K. Shamaei, and Z. Kassas, "Performance characterization of an indoor localization system with LTE code and carrier phase measurements and an IMU," in *Proceedings of International Conference on Indoor Positioning and Indoor Navigation*, September 2019, pp. 1–8.
[53] M. Braasch, "Inertial navigation systems," in *Aerospace Navigation Systems*. John Wiley & Sons, Ltd, 2016.
[54] S. Askari, C. Jao, Y. Wang, and A. Shkel, "A laboratory testbed for self-contained navigation," in *Proceedings of IEEE International Symposium on Inertial Sensors and Systems*, 2019, pp. 1–2.
[55] K. Abdulrahim, T. Moore, C. Hide, and C. Hill, "Understanding the performance of zero velocity updates in MEMS-based pedestrian navigation," *International Journal of Advancements in Technology*, vol. 5, no. 2, pp. 54–60, March 2014.

Ali A. Abdallah (S'13) is a Ph.D. student in the Department of Electrical Engineering and Computer Science (EECS) at the University of California, Irvine (UCI) and a member of the Autonomous Systems Perception, Intelligence, and Navigation (ASPIN) Laboratory. He is a recipient of the Best Student Paper Award at the 2020 IEEE/ION Position, Location, and Navigation Symposium (PLANS).

Chi-Shih Jao (S'20) is a Ph.D. student in the Department of Mechanical and Aerospace Engineering (MAE) at UCI and a member of the UCI Microsystems Laboratory. He is a recipient of 2019 Paul and Beverly Holmes Endowed Fellowships.

Zaher (Zak) M. Kassas (S'98-M'08-SM'11) is an associate professor at UCI and Director of the ASPIN Laboratory. He is also Director of the US DOT **C**enter for **A**utomated Vehicles **R**esearch with **M**ultimodal Assur**E**d **N**avigation (CARMEN). He received a Ph.D. in electrical and computer engineering from the University of Texas at Austin. He is a recipient of the 2018 National Science Foundation (NSF) CAREER Award, 2019 Office of Naval Research (ONR) Young Investigator Program Award, 2018 IEEE Walter Fried Award, 2018 Institute of Navigation (ION) Burka Award, and 2019 ION Col. Thomas Thurlow Award.

Andrei M. Shkel (M'99,F'14) has been a Faculty Member at the University of California, Irvine, CA, USA, since 2000, where he is currently a Professor in the Department of Mechanical and Aerospace Engineering. His professional interests are reflected in more than 260 publications and 3 books. He holds 42 U.S. patents. Dr. Shkel is a recipient of the Office of the Secretary of Defense Medal for Exceptional Public Service for his service as a program manager at DARPA. Dr. Shkel is the President of the IEEE Sensors Council (2020-2021) and an IEEE Fellow.